Solar Energy 272 (2024) 112460

Contents lists available at ScienceDirect

Solar Energy

journal homepage: www.elsevier.com/locate/solener

Green zinc/galactomannan-based hydrogels push up the photovoltage of quasi solid aqueous dye sensitized solar cells

Ana Yancy Segura Zarate [a,b], Lorenzo Gontrani [c], Simone Galliano [a], Elvira Maria Bauer [d], Domenica Tommasa Donia [c], Claudia Barolo [a,e,f], Matteo Bonomo [a], Marilena Carbone [c,*]

[a] Department of Chemistry, NIS Interdepartmental Center and INSTM Reference Centre, University of Torino, Via Gioacchino Quarello 15/a, 10135 Torino, Italy
[b] Escuela de Fisica, Instituto Tecnologico de Costa Rica, Cartago 159-7050, Costa Rica
[c] Department of Chemical Science and Technology, University of Rome Tor Vergata, Via della ricerca scientifica 1, 00133 Rome, Italy
[d] Italian National Research Council-Institute of Structure of Matter (CNR-ISM), Via Salaria km 29.3, 00015 Monterotondo, Italy
[e] ICxT Interdepartmental Center, Università Degli Studi di Torino, Lungo Dora Siena 100, 10153 Torino, Italy
[f] Istituto di Scienza, Tecnologia e Sostenibilità per lo sviluppo dei Materiali Ceramici (ISSMC-CNR), Via Granarolo 64, 48018 Faenza, RA, Italy

ARTICLE INFO

Keywords:
Open circuit voltage
Galactomannan
Zinc-based nanoparticles
Transparency
DSSC

ABSTRACT

In the present work, we implement environmentally friendly water-based Quasi-Solid Electrolytes (QSE) for Dye Sensitized Solar Cells (DSSCs), displaying an unprecedent open circuit voltage (V_{OC}) as high as 750 mV. The production of the hydrogel for QSE-DSSCs is achieved by exploiting the concept of fully green design and fabrication, through the selection of components such as the natural polysaccharide galactomannan (GM), biocompatible zinc salts, and the employment of eco-friendly synthetic procedures to produce the hybrid gelating agents. In the process, moderate temperature (<40 °C), only aqueous solutions are employed, and, at most, ethanol is used in some phases of the procedure. Depending on the type of the initial salt, either zinc hydroxysulfate lamellae or zinc oxide nanoparticles are created within the gel matrix, with a more extended nanoporous structure in the latter case. The nanostructures and the gels are investigated by multiple techniques, including X-ray diffraction (XRD), infrared spectroscopy (IR), scanning electron microscopy (SEM) and thermogravimetric analysis (TGA). Upon ensuing addition of I-/I_3^- redox mediator and assembling of the device, state-of-the-art aqueous QSE-DSSCs are achieved. The latter couples a 2 % efficiency (limited by charge diffusion as proved by Electrochemical Impedance Spectroscopy) with a good Average Visible Transmittance (AVT), and Light Utilization Efficiency (LUE), a couple of coveted features in wave-selective or semi-transparent devices. Finally, Linear Response-Time Dependent DFT (LR-TDDFT) simulations are carried out on a model iodine/iodide layered zinc hydroxy sulphate structure towards a better understanding of the mechanism responsible for the high AVT.

1. Introduction

High performance DSSCs are among the most coveted solutions for direct solar energy conversion to electricity, since they can couple reliability, versatility, low-cost, easiness of fabrication and effectiveness under different light conditions [1–5]. In addition, properties such as shapebility, flexibility, lightweight, transparency, bifaciality and wave selectivity of DSSCs make their aesthetic features attractive in terms of device architecture [6–8], paving the way towards their actual implementation in several present and future applications. Among the most relevant and appealing utilization of DSSCs, one can include Building Integrated Photovoltaics (BIPV) [5,9], Product Integrated Photovoltaics (PIPV) [10,11], Agrivoltaics [8], let alone aerospace [12]. Most important, DSSCs rely on the exploitation of sustainable devices components, free from critical raw materials (CRM-free), as dye/absorber, electrolyte and counter-electrode [13–16], at variance with other emerging photovoltaic technologies, including Perovskite Solar Cells. The pathway of sustainability implementation goes through the employment of an environmentally friendly electrolyte, i.e. a key component for both photovoltaic performance and long-term stability of DSSCs. Traditionally, highly efficient electrolytes are based on organic solvents, *e.g.* acetonitrile, valeronitrile, and 3-methoxypropionitrile, that are oil-derived, possess high flammability and volatility, thus inevitability leading to safety issue and electrolyte leakage over time. Water has been

* Corresponding author.
E-mail address: carbone@uniroma2.it (M. Carbone).

https://doi.org/10.1016/j.solener.2024.112460
Received 29 November 2023; Received in revised form 4 March 2024; Accepted 10 March 2024

proposed as the ideal low-cost, non-toxic, safe and environmentally friendly alternative to replace conventional organic-based electrolytes in dye-sensitized solar cells [17–19]. One of the main drawbacks generally observed in aqueous DSSCs (a-DSSC) is a rather low V_{OC}, i.e. around 0.4–0.6 V, to be compared to organic electrolytes (>0.7 V), in case I-based electrolyte is employed. Many reasons have been proposed to explain the decrease in V_{oc}, such as the negative shifting of the conduction band potential of the semiconductor layer, the lowering of redox mediator potential, and the increasing of charge recombination between injected electrons in semiconductor layer and the dye/mediator [20–23]. Although there are numerous studies focused on increasing the voltage in DSSCs with organic electrolytes [24–27], research on I-based aqueous DSSCs is much more limited, and there are only few articles in the literature. For example, some adopted strategies are the treatments of the TiO_2 mesoporous layer, the use of purposely designed dyes [28], the introduction of additives and surfactants into the electrolyte [17,22,28,29], the use of different iodide/iodine concentrations and sources [18,20,22,28,30]. Despite these efforts, up to now, only two studies on liquid iodine-based aqueous electrolyte show a V_{OC} up to 0.74 V, i.e. comparable with high-performing organic DSSCs [17,31]. Such low voltages still limit the possibility to integrate a-DSSCs with energy storage systems, i.e. batteries and supercapacitors, and other smart Internet of Things (IoT) devices. Hence, an improvement of V_{OC} is warmly demanded for the industrialization of a-DSSCs and the development of light-powered integrated smart devices.

Another shortcoming of the employment of water as liquid electrolyte is leakage that cannot be completely ruled out despite its low vapour tension. One of the most elegant strategies to solve this problem and to improve the long-term stability of DSSCs is using water-based quasi-solid electrolytes (QSEs), or hydrogels, made by incorporating or trapping the aqueous electrolyte into a hydrophilic matrix or framework. This way, it is possible to exploit suitable gelling agents that possess the diffusive property of liquids and the cohesive property of solids [32]. The choice of the gelating agents is pivotal, both to the DSSC performance and to their overall sustainability, also taking into consideration the abundance of the materials used for their production. Among organic polymers, biopolymers, *e.g.* polysaccharides [33], derived from natural and renewable resources are drawing much attention, since they are the best choice in developing more sustainable DSSCs due to their abundance, reduced carbon footprint, low-cost and facile production [34]. More recently, hybrid QSEs based on both organic and inorganic gelling agents have been successfully proposed in DSSCs with mixed aqueous/organic solvent, demonstrating higher conductivity and chemical capacitance, lower charge transfer resistance and charge recombination, and longer electron lifetime [35,36]; however, reports on fully aqueous hybrid QSEs are still missing in literature so far. On these grounds, efficient hybrid aqueous QSEs based on biopolymers and low-cost additives appear necessary for the development of truly sustainable, stable, and performing DSSCs. Therefore, in the present work, we sought a suitable hybrid gelating system, aiming at: *i)* a better trade-off between photovoltaic efficiency and device transparency, *ii)* environmental friendliness, *iii)* sustainability of the whole synthetic process. More in detail, we synthesized, characterized, and employed in DSSCs, aqueous quasi-solid electrolyte based on galactomannan (GM) biopolymer and zinc oxides/hydroxysulphates nanoparticles and lamellae. The ensuing I^-/I_3 charged aqueous gels were implemented as fully green electrolytes into lab-scale solar cells leading to devices, that show state-of-art photoconversion efficiency, driven by a remarkably high photovoltage hitting 750 mV, a never-reached value in QSE aqueous DSSCs based on iodinated electrolyte. Seeking wave-selectivity or semi-transparency of photovoltaic devices [7], the quest for high efficiency should be coupled with a moderate absorption throughout the visible spectrum (i.e. between 400 and 700 nm). In this regard, a new figure of merit, namely Light Utilization Efficiency (LUE) [37] has been recently proposed, that is measured as the product between the Photoconversion Efficiency (PCE) and the Average Visible Transmittance (AVT) of the cell. The Zn/GM electrolytes we propose, exhibit a promising AVT up to 22 %, with improved transparency between 500 nm and 750 nm, and an ensuing LUE, that is more than doubled in comparison to xanthan gum-based reference.

As for the sustainability of the DSSC devices and their production process, a few considerations are in order. Galactomannans are natural and abundant polysaccharides available in legume seed endosperm with multidimensional aspects which are cost-effective and eco-friendly. The chemical structure is formed by a linear chain of β-(1–4)-D-mannan backbone with single D-galactose branches attached at α-(1–6) position. The ratios of galactose and mannose varies from 1:1 to 4:1 depending on the sources of polysaccharides (Fig. 1) [38]. The galactomannans are versatile materials for various applications such as binding, emulsifying, gelling, suspending, thickening and coatings [39].

ZnO is a fully sustainable, green material, that is routinely used in products for children skin care, sunscreen products, dentistry, among all applications. It can be synthesized in eco-friendly conditions [40] and can be swiftly disposed and recycled [41]. Zn-based nanomaterials, in general, are often considered as having low environmental impact, especially in those cases when the potential threat is related to the leakage of harmless Zn^{2+}.

In pursuing the goal of achieving highly efficient but sustainable water-based QSE-DSSCs, a fully green route has been adopted in the synthesis of the gelling agent. Indeed, the whole synthetic procedure is carried out employing aqueous solutions, or ethanol, at most, at relatively low temperatures (a maximum of 40 °C was adopted) [40], thus enhancing the sustainability impact. Furthermore, several synthetic parameters were explored, such as Zn salts and Zn-based NPs/GM ratios to ensure the best performing combination.

In conclusion, the hydrogel electrolytes proposed here represent a step forward towards the development of aesthetic and sustainable dye-sensitized solar cells.

2. Results and discussion

The first step of the fabrication of a QSE-DSSC is the achievement of the ZnNPs-based gelling agents. To this aim, a thoughtfully designed procedure was implemented (see experimental section 3.2 for further details), ensuring environmental friendliness, low-cost and smooth execution. These requirements resulted in a one-pot procedure, carried out in aqueous solution, either at room temperature or at 40 °C at most, where the gel forms during the final centrifugation step. A few parameters were varied, i.e. Zn salt (nitrate or sulphate), Zn concentration (0.1 M or 0.02 M) and Zn/GM ratio (1:0.5, 1:1, 1:2), aiming at finding the best conditions for tuning their physical–chemical properties. Overall, more samples were synthesized with different Zn/GM rations and Zn concentrations. Here we report only those with comparable consistencies and highest water content. For investigation purposes, dries samples were achieved as well. A table with the synthetic conditions and subsequent samples' naming is reported in the Supplementary Information (Table SI1). As a general rule, the letter G in the sample code identifies a gellified compound, whereas the dried counterparts are labelled with acronyms starting with the letter D. In addition, the letter A indicates sulphate derived samples, the letter B, the nitrates derived

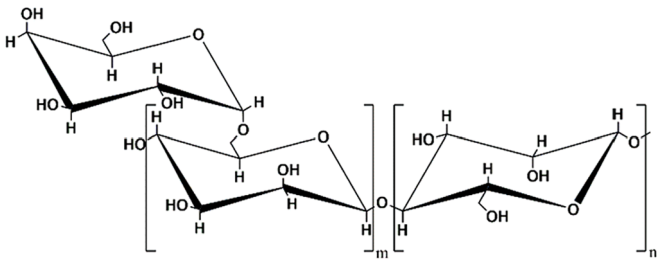

Fig. 1. Molecular structure of galactomannan.

ones. Once the experimental parameters had been set up and the synthesis of Zn-based NPs performed, a thorough structural and morphological characterization was carried out both on gels and on the dried samples, to determine crystalline phases, stability, texture, and possible NPs formation. The drying of the samples was necessary for investigations by XRD, since the presence of aqueous gelly galactomannan overwhelms the features of embedded nanocrystallites, with an ensuing broad amorphous pattern (Fig. S1). The XRD patterns of the dried samples are reported in Fig. 2. Panel A refers to the sulphate-derived samples, i.e. D-A1, D-A2, D-A3 synthesized with GM at different ratios, namely 0.5 %, 1 % and 2 % w/V, respectively (see section 3.2.1, for more experimental details). In panel B, the XRD pattern of the nitrate-derived samples are reported, i.e. DB-1 and DB-2, obtained at lower Zn concentration and GM at 0.5 % and 1 % respectively, small and DB-4 achieved at higher Zn concentration and GM at 0.5 % and 1 %, respectively (see section 3.2.2, for more experimental details). In analyzing the patterns, however, it must be considered that the drying process may also induce $Zn(OH)_2$ to ZnO transition following on from dehydration pathways, leading to an underestimation of the former phase, whether present in the gel.

The spectra are characterized by several broad peaks, due to the presence of galactomannan and to the possible superposition of different inorganic phases (see below). For this reason, the spectrum of GM, measured separately (reported as Supplementary Information, Fig. S2), was subtracted from the profiles as baseline. Features around 28°, 33°, 37°, 42°, 56°, 59° and 63° 2θ degrees (Cu radiation), appear in all the spectra, though they are more evident in D-A3 and more blurred in the others. In addition to this, all the spectra display a distinct peak at low angle, i.e. in the 8.5–9.5 degrees range, that is related to distances in the range 1–10 nm, as it occurs, for instance, in layered structures. Therefore, the ensuing identification of the phases was performed, according to the Rietveld procedure as implemented in the software GSAS-II [42], based on the three known stable phases of layered zinc hydroxy sulphate (basic sulphate) minerals for the fitting: lahnsteinite $Zn_4(SO_4)(OH)_6{\cdot}3H_2O$ (triclinic) [43], namuwite $Zn_4(SO_4)(OH)_6{\cdot}4H_2O$ (trigonal) [44] and osakaite $Zn_4(SO_4)(OH)_6{\cdot}5H_2O$ (triclinic, mineral [45] and synthetic analogue [46]). These three minerals differ by the number of water molecules of crystallization and belong to the same Nickel-Strunz classification [47], namely the 07 class (sulphates), containing additional anions and water molecules. They share the same basic brucite-like crystal structure of layered hydroxy salts (LHS) [48–51], which features sheets of edge-sharing ZnO_6 octahedra with a fraction of Zn^{2+} cations (one seventh) not occupying the octahedral sites (i.e. one every sixth site is vacant) but placed, instead, in tetrahedral sites below and above each empty octahedron, grafted with sulphate anions. This bidimensional structure is described as “decorated interrupted-layers” [52], and a variable number of water molecules can intercalate between the layers [53], with possible interconversion between the various forms upon hydration/dehydration [54]. Among lahnsteinite, namuwite and osakaite, the last two systems gave a similar agreement with experimental data in the Rietveld fit, with a slightly better score in namuvite case, which is reported as “fit” plot in Fig. 2. The reflections of the three mineral phases are reported as vertical ticks: namuwite (light green), osakaite (purple), lahnsteinite (blue-violet). Despite the satisfactory agreement found with hydroxysulfates, the contribution to the scattering coming from zinc hydroxide or oxide phases, that could be present in small quantities in the three patterns, cannot be completely excluded, considering the large number of faint peaks in the XRD profile.

The patterns of all nitrate derived samples reveal the presence of ZnO, as it can be ascertained by the high complementarity between the observed peaks in the dried gels and hexagonal ZnO reflections, whose high intensity “triad” at 32.0°, 34.5° and 36.3° degrees (corresponding to the reflections from 100, 002 and 101 planes, respectively) can be easily spotted in all the four samples, together with the smaller signals falling at higher angles. Additionally, a $Zn(OH)_2$ phase seems to be present as well, considering the baseline rise in D-B1 and D-B2 and the presence of definite peaklets/shoulders at 34° and 57° in D-B3 and D-B4. The Rietveld fit of the structure, using hexagonal zincite and orthorhombic $P2_12_12_1$ Wülfingite as crystal phases, and the ratio between the two (i.e. oxide:hydroxide) as one of the fit parameters suggests that the hydroxide accounts to about 1–2 % of the phase fraction.

Gels and dried samples were comparatively analyzed by IR spectroscopy. The outcomes are reported in Fig. 3, along with reference spectra of GM and of purposely synthesized $Zn(OH)_2$ and ZnO. The full assignment of the GM features [55] is reported in Table SI2 of the Supplementary Information. The subsequent analysis of the spectra has been carried out to determine whether *i)* the GM is present or has undergone undesired processes, *ii)* $Zn(OH)_2$ and/or ZnO formed in nitrate-derived samples (gels and dried) *iii)* hydroxide sulphate structures are present in sulphate-derived samples.

As far as the gel samples are concerned, (G-A1 through G-A3 and G-B1 through G-B4, Fig. 3), it can be ascertained that all of them contain a consistent amount of water, both adsorbed and intercalated, as evidenced by the relatively higher intensity of the OH stretching and bending vibrations, at 3250 cm^{-1}, 1640 cm^{-1} and below 800 cm^{-1}, as compared to reference GM. In addition, the –OH stretching band is

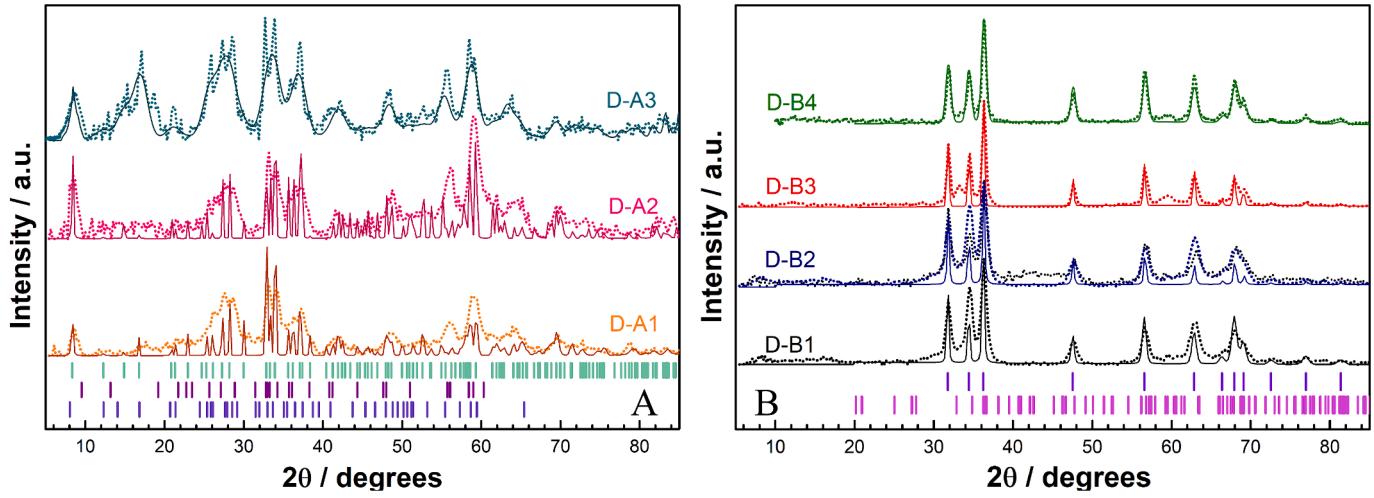

Fig. 2. XRD pattern of the dried samples. Panel A: sulphate-derived samples. The vertical lines at the bottom correspond to namuwite (light green), lahnsteinite (purple), and osakaite (blue-violet) crystal reflexes. Panel B nitrate-derived samples: the vertical lines correspond to ZnO (violet) and $Zn(OH)_2$ (magenta). Dots: experimental data; continuous file: Rietveld fit. (For interpretation of the references to color in this figure legend, the reader is referred to the web version of this article.)

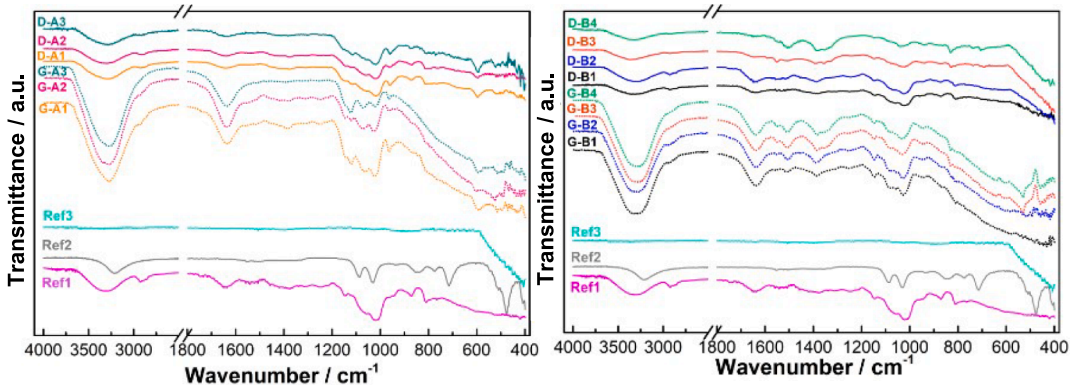

Fig. 3. IR spectra of synthesized gels and dried samples. Panel A: sulphate-derived samples; panel B: nitrate-derived samples.

slightly shifted towards lower wavenumbers, indicating changes in the hydrogen-bonding network of the gellified materials. Furthermore, in all gels, the typical bands of GM can be observed, i.e. the $–CH_2$ stretching vibrations below 3000 cm^{-1}, absorbances between 1100 and 1000 cm^{-1} and several shoulders below 800 cm^{-1}, thus indicating the preservation of the polysaccharide in the synthetic procedure.

More in detail, as far as the nitrate derived gels are concerned, the presence of $Zn(OH)_2$ cannot be clearly ascertained, because of the overlap with the features of GM. Indeed, the characteristic peaks of $Zn(OH)_2$, visible in the reference spectrum of Fig. 3. i.e. the prominent vibration peaks at 3220 cm^{-1} (–OH stretching), 1086, 1029 and 933 cm^{-1} (Zn-OH bending), 847, 774 and 715 cm^{-1} (–OH librations) and 478 cm^{-1} (Zn-O stretching) fall in regions where also the GM features appear, thus hiding them. The presence of ZnO is rather evident in high Zn-content samples (G-B3 and G-B4 in Fig. 3), where the Zn-O stretching vibration appears around 410 cm^{-1}. This characteristic feature, however, is partially masked by GM bands in low Zn-content samples [40]. As a general consideration, although $Zn(OH)_2$ is not unequivocally detected, it is quite likely to form on the surface of ZnO particles, due to the large amount of water in the gels.

Gels derived from sulphates display quite intense vibrations at 1078 cm^{-1} and 1120 cm^{-1}, and a shoulder at 1148 cm^{-1}, in association with less intense and broad peaks at 960 cm^{-1}, 600 cm^{-1} and 450 cm^{-1}. These features are typical for low symmetry sulphate ions (SO_4^{2-}) and originate from the ν_3 band with T_d symmetry, generally located around 1000 cm^{-1}, that splits for a symmetry lowered towards C_{3v} as in the case of monodentate bonding of the sulphate ion [56]. In addition, the ν_1 sulphate band, around 950 cm^{-1}, becomes IR active, for lower symmetries. The observed spectral features account for the presence of the aforementioned basic zinc sulphate(s) [45,46].

As for the dried samples, the ones derived from nitrates do present a broad peak below 600 cm^{-1} (a declining slope towards the edge of the spectra), related to formation of ZnO, that has a higher intensity in the samples at a higher Zn content (D-B1 and D-B2, Fig. 3). GM related features are all present, as well.

In the sulphate-derived samples, the water content visibly diminishes, upon drying, whereas the GM features remain. Interestingly, the peaks assigned to zinc hydroxide sulphate and especially the ν_3 and ν_4 vibrations are still visible after drying, though at a lesser extent, indicating the persistence of the LHSs structures. Distinct formation of zinc hydroxide or zinc oxide cannot be ascertained due either to lack of corresponding characteristic signals, or to their coverage by GM features, that are present as well.

SEM imaging of hydrogels is typically limited by the loss of moisture under the vacuum conditions necessary for the measurements. Therefore, several samples preparation techniques have been adopted to retrieve morphological information. Here, we took images from gels subjected to freeze-drying, and, in addition, we implemented the method proposed by Fasiku et al. [57] that consists in depositing the hydrogel on a silicon sample holder, let it dry shortly and remove the sample in excess, with filter paper prior to the imaging. Furthermore, we took images of the previously dried, powder samples, deposited on carbon-tape. In Fig. 4, the images of the samples G-A1, G-B1, D-A1 and D-B1 are reported, i.e. sulphate derived at low GM content (0.5 % GM), both gel (G-A1) and dried (D-A1), and nitrate derived at low Zn concentration (i.e. the same used for the synthesis with sulphates), and low GM concentration (GM 0.5 %), both gel (G-B1) and dried (D-B1). However, similar images were obtained from the other sulphate and nitrate derived samples. More in detail, left panels (4a and 4d) are G-A1 and G-B1 subjected to freeze-drying, central panels are G-A1 and G-B1 deposited by quick-drying (4b and 4e) and the right panels are images of D-A1 and D-B1 (4c and 4f). By freeze-drying, it can be appreciated how both sulphate and nitrate-derived gels display a rough surface, though the former appear more compact whereas the latter present a clear nanoporosity.

The quick-drying method allows images with more details of the inherent structures, and remarkably shows lamellar formations from G-A1, fully compatible with the LHS structure of namuwite/lahnsteinite/osakeite, hypothesized basing on the IR and XRD spectra. As for G-B1, upon gel quick-drying, distinct NPs could be imaged with average diameters in the 30–60 nm range. Finally, imaging of D-A1 and D-B1 indicates that lamellar and spherical structures are, respectively, retained upon drying the hydrogels overnight at 50 °C. The latter have a larger average diameter with respect to the hydrogel, clearly, due to the coating by GM, upon drying.

The thermal profile of the hydrogels was investigated by thermogravimetric analysis (TGA) and graphically reported in Fig. S3. All nanocomposite hydrogels exhibit a single stage thermal decomposition, ending at temperatures in the range 73–85 °C (sulphate-derived gels), and 85–95 °C (nitrate-derived gels). The residues are 10 % and 5 % weight, respectively. The large weight losses at relatively low temperatures suggest that the gels incorporated large amounts of water, that are released in a one-step detachment together with the galactomannan, and that the polymer has a low cross-linking, probably due to the mild synthesis conditions. The decomposition of the nitrate-derived gels at slightly higher temperatures (especially G-B4) hints at stronger intermolecular connections, that can be related to a better coordination around the ZnO-NPs. Finally, the higher residue, in the case of the sulphate-derived samples, as compared to the nitrate ones, correlates to the entrapment of residual ions between the layered structure.

Once the investigations of the gels have been completed, the latter were loaded with the redox mediator (i.e. 0.5 M in NaI and 0.03 M in I_2) and implemented as QS electrolyte in a-DSSCs, using D131 as dye, whose molecular structure is reported in Fig. S4 of the Supporting Information. The corresponding devices are labelled with the gel acronym followed by "-I". In Fig. 5, the figures of merit of the different devices are compared to each other and the photovoltaic figures of merit of the most performing ones are summarized in Table 1.

Such impressive V_{OC} values are counterbalanced by relatively low

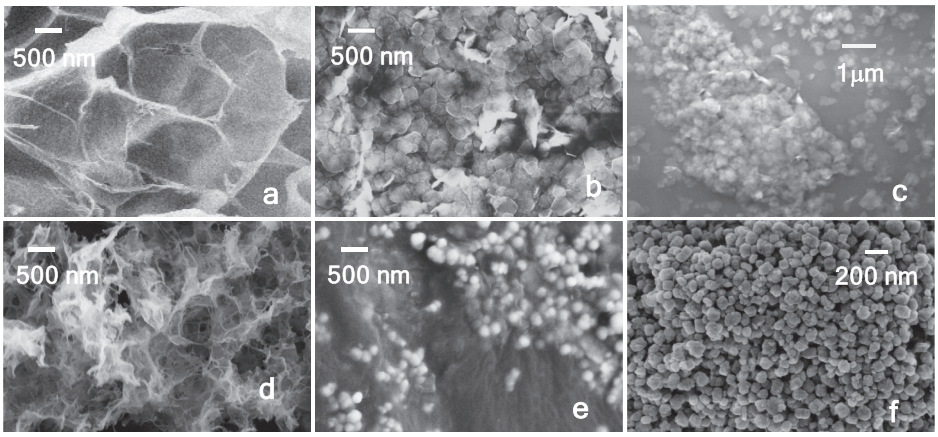

Fig. 4. SEM images of sulphate-derived samples (top panel) and nitrate-derived samples (bottom panel): a) G-A1 subjected to freeze-drying, b) G-A1 subjected to quick drying, c) D-A1, d) G-B1 subjected to freeze-drying, e) G-B1 subjected to quick drying, f) D-B1. For the gels, the same magnifications were used, whereas the magnification is different for the dried sample, for better appreciating the peculiar structures.

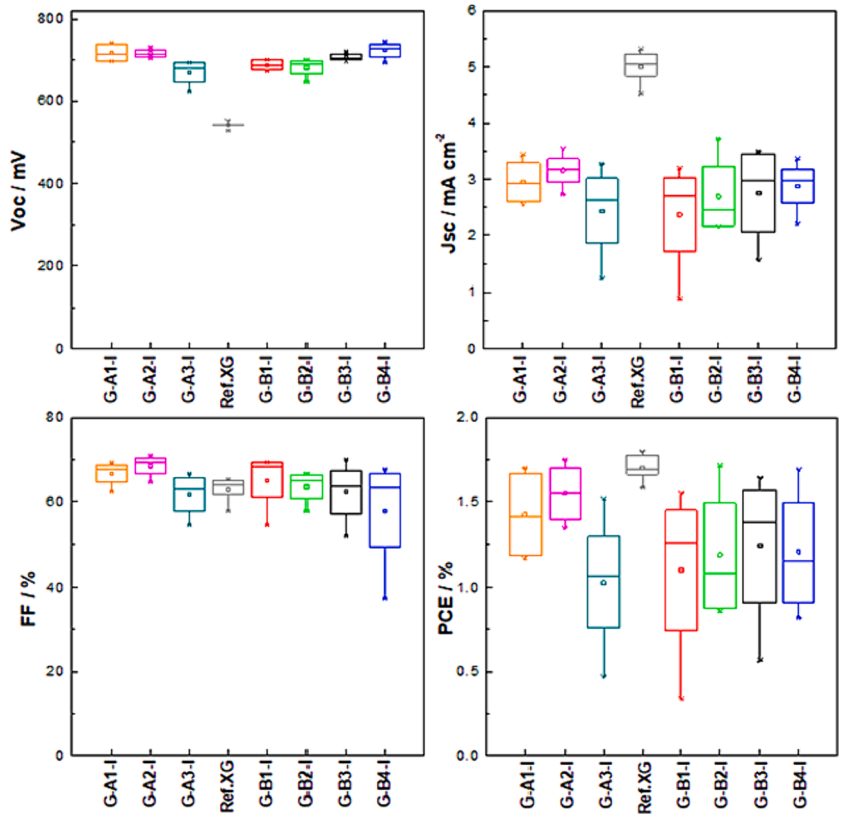

Fig. 5. Photoelectrochemical figures of merit, i.e. V_{oc} (top left), J_{sc} (top right), FF (bottom left) and PCE (bottom right), for a-DSSCs fabricated with all the gels described throughout the paper.

photocurrent density (J_{SC}) values that do not exceed 4 mA cm^{-2} (for the best cell, G-B2-I) whereas the J_{SC} of the reference cell is stable around 5 mA cm^{-2}. As a result, all the proposed gels, but G-A3-I, allow to emulate the photoelectrochemical behaviour of the XG-based reference system (ref-XG). It must be noted that in the present electrolyte, we opted to not implement the chenodeoxycholic acid (CDCA) as anti-aggreging agent into the electrolytes, that it is, instead, present in ref-XG, although it is known to improve the performances of the photovoltaic devices minimizing the recombination reaction involving the redox mediator at the photoanode/electrolyte interface [18]. Our choice is based on overall greenness of the proposed device, as CDCA does not represent an environmentally harmless component. Thus, we are fairly convinced that further optimization of our electrolyte could lead to even better results, paving the way towards new NPs-aqueous gel electrolytes for truly green and sustainable a-DSSCs. Indeed, our devices showed comparable results with state-of-the-art references, whose figures of merit are summarized in Table 2.

Compared to other G-AX-I gels, G-A3-I differs for a higher amount of GM (2 %w, in the preparation phase) and for a higher viscosity.[1] Thus,

[1] We could not measure the exact values of viscosity, because repeated tests resulted in a phase separation of liquid and solid components, in our experimental set-up.

Table 1
Photovoltaic figures of merit of the most performing QS aqueous DSSCs.

Device	V_{OC} / mV	J_{SC} / mA cm^{-2}	FF / %	PCE / %
G-A1-I	731	3.425	68.0	1.702
G-A2-I	718	3.533	69.0	1.752
G-A3-I	693	3.272	66.7	1.515
Ref-XG	551	5.240	61.8	1.780
G-B1-I	702	3.185	69.4	1.550
G-B2-I	696	3.719	66.2	1.710
G-B3-I	721	3.496	65.1	1.640
G-B4-I	746	3.350	67.6	1.690

For sake of completeness, all the J-V curves are reported in Fig. S5. Even at a first glance, one can see how the open circuit voltage (V_{OC}) obtained with Zn-based gel electrolyte is much higher than the one obtained with reference electrolyte (i.e. Xanthan-gum based gel), increasing from 540 mV up to 746 mV (for G-B4-I, average values), that is, as far as we are aware, the highest value ever reported for I-based aqueous DSSCs (see Table 2).

we carried out some Electrochemical Impedance Spectroscopy (EIS) analyses of symmetric (i.e. FTO-Pt/electrolyte/Pt-FTO) devices made of G-AX-I gels to analyze the charge transfer at the electrode/electrolyte interface and the diffusion kinetics throughout the gel electrolyte. EIS spectra in the form of Nyquist's plots are reported in Fig. S6. The latter have been interpolated using a conventional equivalent circuit (inset of Fig. S6) made up of a series resistance (modelling the circuital elements external to the cell), a resistor with a capacitor connected in parallel to model the charge transfer kinetics at the electrode/electrolyte interface and a Warburg (open) element associated to the diffusion of the mediator throughout the electrolyte. Once EIS spectra are interpolated using this equivalent circuit, it could be evidenced how the higher the amount of GM in the gels, the larger the second semicircle in the impedance plot, which accounts for the diffusion resistance (or Warburg resistance, R_W) experienced by the ions in diffusing throughout the electrolyte. More in detail, the R_W is 10 Ω, 12 Ω and 16 Ω for G-A1-I, G-A2-I and G-A3-I, respectively and it always larger than the one of the reference symmetric cell using XG as electrolyte (i.e. 5 Ω). These data evidence that ions experience higher resistance in diffusing throughout the electrolyte because of the higher viscosity of G-A3-I, as commonly observed with other type of hydrogels [64].

On the other hand, any meaningful difference could be seen when the first semicircle of the impedance (ascribable to the electrode/electrolyte interfacial charge transfer, R_{CT}) is analyzed; indeed, R_{CT} values range from 0.5 Ω for XG and G-A1-1 to 1.5 Ω for G-A2-I and G-A3-I. Going into details with the behaviour of chemical capacitance (C_μ, extracted from the interpolation of the constant phase element, CPE), one could note that the differences between the devices are within the errors (see table SI3). Following on from this, we can speculate that the quality of electrode/electrolyte interface and the number of interfacial charges (i.e. quantity and chemical nature of the ion at the first interface) is not impacted by the nature of the gelling agent. As a final remark, EIS analyses allow to prove that the lower current density of G-AX-I (and especially G-A3-I) could be mainly related to charge diffusion limitation. The analyses reported above proved a detrimental effect of the increase of GM concentration on the photovoltaic efficiency of the resulting devices. Thus, moving to gel electrolytes based on pure ZnO NPs (*e.g.* G-BX-I), we resolve to exploit only the 0.5 and 1.0 % w/w composition. As one can see in Fig. 5, G-BX-I electrolytes leads to slightly lower photoconversion efficiency compared to G-AX-I counterparts, mainly related to a decreased FF (samples G-B3-I and G-B4-I) or V_{OC} (samples G-B1-I and G-B2-I).

Aiming at highly transparent and colour-neutral devices, the spurious absorbance of the electrolyte [65] is very detrimental to the LUE because it negatively affects the AVT without influencing the PCE. To estimate the AVT (and thus the LUE), we proceeded to measure the transmittance in the visible range of complete devices filled with the different hydrogels (Fig. 6). The UV–Vis spectra of complete cells are reported in Fig. S7. One should note how G-A3-I showed the highest AVT (≈ 22 %), decreasing with the amount of GM in the gels (AVT ≈ 20 % and 13 %, for G-A2-I and G-A1-I, respectively). On the other hand, the presence of pure ZnO NPs in the gels leads to even lower AVT values (between 6 % and 11 %). When PCE and AVT data are compared, it appears that the G-A2-I device shows the highest LUE, i.e. 0.35 %, outperforming the XG-based reference devices (LUE = 0.14 %).

Screening the literature, a similar effect has been dcscribed for hybrid electrolytes based on a mixture of I^-/I_3 and thiolate/disulphide or more complex S-based systems (i.e. sulphates) [66,67]. Thus, aiming at disclosing the reason behind the higher transparency of the hydroxy-sulphate gels (A-series) we performed some computational analyses. To this purpose, we employed a model where iodine and iodide fragments interact with the sulphate anions attached to the brucite-like layers and dangling towards the interlayer space, as well as with water molecules present in the same space (Fig. S8). The interaction was modelled considering a sulphate anion and an iodine (iodide) molecule (anion) as the minimal aggregate, while the presence of water was simulated using the PCM continuum model. The same type of calculation protocol was applied to bare molecular iodine and iodide anion in PCM water, in order to evaluate the sulphate coordination effect. The geometry of the configurations was optimized, and the UV–Vis absorption spectrum was calculated according to the LR-TDDFT method. Two different Density Functionals were employed that are often used to calculate the optical properties of dyes and other materials of technological interest (M06 [68] and CAM-B3LYP [69]), using DGDZVP as basis set [70]). The latter, in particular, has proved to be suited for studying intermolecular interactions in halogen atoms (halogen bonding). The main parameters of the optimized structures are reported in the table below (Table 3) with calculated distances in Å and wavelengths of the lowest energy vertical transition in nm. Further details are given in the Supplementary Information.

From the inspection of the results, it appears clear that the interaction between iodine and sulphate leads to a strong electrophile–nucleophile (anion) interaction, with the establishment of a short contact between one iodine atom and one sulphate oxygen atom in all the models (Fig. S9). Such interaction leads to a modification of iodine

Table 2
Dye, gelators, additives, iodide source, and photovoltaic figures of merit of I-based QS aqueous DSSCs reported in literature.

Dye	Gelator	Additive	I⁻-source	V_{OC} / mV	J_{SC} / mA cm^{-2}	FF / %	η/%	Ref.
–	agarose	–	KI	670	3.27	24	0.54	[58]
D907	PEG	TBP	BMIM-I	600	2.1	44	0.6	[59]
D907	P123	TBP	BMIM-I	490	4.6	57	1.3	[59]
D907	F77	TBP	BMIM-I	595	6.2	53	2.1	[59]
SK3	F77	TBP	LiI	690	4.76	61	2.0	[60]
D131	NaCMC	–	NaI	437	2.33	60	0.61	[61]
D131	NaCMC	–	KI	453	2.61	61	0.72	[61]
D131	Lignin-PEGDGE	CDCA	NaI	634	3.62	67	1.54	[62]
D131	Xanthan	CDCA	NaI	638	4.95	68	1.93	[63]
D131	Xanthan	CDCA	NaI	551	5.24	62	1.78	This work
D131	Zn-based NPs	–	NaI	746	3.35	68	1.69	This work

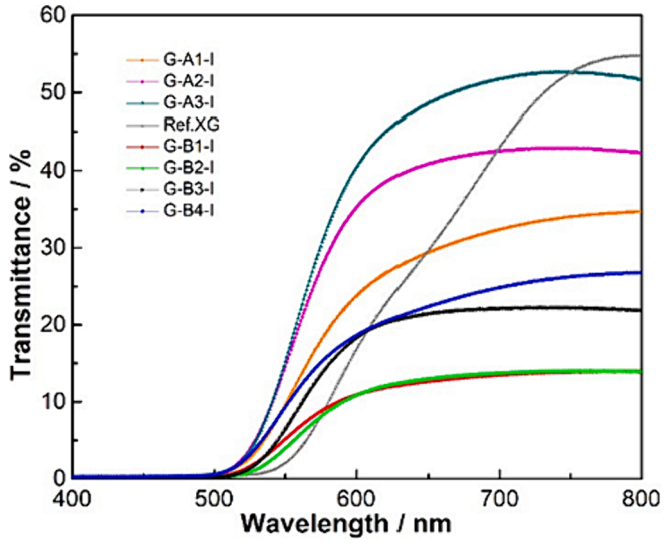

Fig. 6. Transmittance spectra (in the visible range) for aqueous DSSCs made by the different gels exploited throughout the paper.

Table 3
Relevant geometrical parameters and absorption data of the $SO_4 - I_2/I_3^-$ models. Distances in Å, wavelengths in nm.

Method -\ System		I_2	I_3^-	SO_4 - I_2	SO_4 - I_3^-
M06/DGDZVP	d I-I	2.6914	2.95404	2.9183	2.8959
	d (S)O···I			2.2473	2.2740
	d I_2···I				4.5310
	Highest λ	517.25	461.84	374.4	411.32
CAM-B3LYP/ DGDZVP	d I-I	2.7183	2.9874	3.4424	2.9569
	d (S)O···I			2.08853	2.2527
	d I_2···I				15.6413
	Highest λ	541.53	483.63	396.07	390.5

and iodide UV–Vis absorption spectra, that undergo a general blueshift. The lowest energy transitions (highest λ), that are predicted as mainly HOMO-LUMO in character by the TD-DFT algorithm, are reported in Table 3, whereas the full spectra of 30 transitions is reported in the Supplementary Information (Figs. S10 and S11).

Finally, we monitored the evolution of the a-DSSCs' photoelectrochemical figures of merit over time, in order to assess the stability of the devices also compared to ref-XG. This analysis was limited to hydroxysulphate-based cells, since they are the most efficient. As one can see from Fig. 7, stable PCE values are reached with G-A1-I and G-A2-I, even as soon as the device is assembled. On the other hand, G-A3-I reaches its maximum after 1 day of ageing, this being likely related to the higher viscosity of this electrolyte leading to a longer time needed to diffuse throughout the mesoporous structure of the photoanode and to properly wet it [71,72]. Such a behaviour is even more evident looking at the ageing of ref-XG, which requires 48 h to reach the highest efficiency. The longer "activation" time could be ascribed to both a higher viscosity of ref-XG as well as to its more hindered structure that would lead to a slower stabilization of the photoanode/electrolyte interface. G-AX-I systems show a lower stability compared to the reference device, with G-A1-I (the more stable among new gels and the one with the lowest GM content) showing a halving (-50 %) of its initial efficiency after more than 500 h. On the other hand, ref-XG only loses less than 20 % of its maximum efficiency in the same timeframe. These issues open the way for further developments of the sugar-based components towards the optimization of the activation/lifetime of the system.

3. Experimental section

3.1. Materials

Zinc nitrate ($Zn(NO_3)_2{\cdot}6H_2O$-CAS No.10196-18-6), zinc sulphate ($ZnSO_4{\cdot}7H_2O$-CAS No 7446-20-0) sodium hydroxide (NaOH CAS No 1310-73-2), sodium iodide (NaI, CAS No. 7681-82-5), iodine (I_2, CAS No. 7553-56-2), chenodeoxycholic acid (CDCA, CAS No. 474-25-9), absolute ethanol (EtOH, CAS No. 64-17-5), acetone (CAS No. 67-64-1), *tert*-butanol (t-BuOH, CAS No. 75-65-0), isopropanol (2-prop, CAS No. 67-63-0), 2-Cyano-3-[4-[4-(2,2-diphenylethenyl)phenyl]-1,2,3,3a,4,8b-hexahydrocyclopent[b]indol-7-yl]-2-propenoic acid (D131 dye), fluorine doped tin oxide coated glass slide (FTO glass, surface resistivity ~ 7 Ω sq^{-1}), titanium tetrachloride ($TiCl_4$, CAS No. 7550-45-0), chloroplatinic acid (H_2PtCl_6, CAS No. 16941-12-1), Galactomannan (CAS No. G0753) and acetonitrile (ACN, CAS No. 75-05-8) were purchased from Sigma-Aldrich. Deionized water (DI-H_2O, 18 MΩ cm at 25 °C) was obtained with a Direct-Q 3 UV Water Purification System (Millipore). TiO_2 paste purchased from (DSL 18 NR-T, Dyesol).

3.2. Synthesis

The biopolymer mediated synthesis of the Zn-based nanocomposites was carried out by *in situ* chemical precipitation procedure according to Bouttier-Figueroa [73] and to Donia [40,74–76] with some modifications.

3.2.1. Gels from Zn sulphate

Aqueous solutions at different GM concentrations (0.5, 1, 2 % W/V) were prepared in 50 mL of deionized water and stirred at room temperature for 24 h. Upon complete GM dissolution, zinc sulphate ($ZnSO_4{\cdot}7H_2O$) was added to achieve a concentration of 0.02 M and the solution was left under stirring for 2 h. Afterwards, 50 mL of NaOH 0.02 M were added dropwise (1:1 v/v ratio). In a few minutes the reaction mixture appeared opalescent. The solution was left under continuous stirring overnight at room temperature. Finally, absolute ethanol was added (1:2 v/v ratio) and the solution left static at room temperature for 2 h. The GM-nanocomposite gel formed during the ensuing centrifugation, that was carried out for 10 min, at 3500 rpm and 25 °C. For characterization purposes, a portion of the GM-nanocomposite was collected, washed once with DW and dried in oven at 50 °C for 24 h (dried samples). This procedure led to the samples labelled G-A1, G-A2, G-A3, (gels) and D-A1, D-A2, D-A3 (dried powders).

3.2.2. Gels from Zn nitrate

Aqueous solutions at different GM concentrations (0.5, 1 % w/v) were prepared in 50 mL of DW for each one and stirred at room temperature for 24 h. Upon complete GM dissolution, zinc nitrate ($Zn(NO_3)_2{\cdot}6H_2O$) was added to achieve the target concentrations, i.e. 0.1 M or 0.02 M and the solution was left under stirring for 2 h. The solution was thermalized in an oil bath at 40 °C and vigorously stirred for 2 h. Afterwards, 50 mL of NaOH 0.1 M or 0.02 M, depending on the Zn nitrate concentration, (1:1 v/v ratio) were added dropwise and the solution was left under vigorous stirring overnight at 40 °C. The GM-nanocomposite gel formed during the ensuing centrifugation, that was carried out for 10 min, at 3500 rpm and 25 °C. For characterization purposes, a portion of the GM-nanocomposites was collected, washed once with DW and dried in oven at 50 °C for 24 h (dried samples). This procedure led to the samples labelled G-B1, G-B2, G-B3, G-B4, (gels) and D-B1, D-B2-1, D-B3, D-B4, (dried powders).

3.2.3. Reference $Zn(OH)_2$ and ZnO samples

50 mL of an aqueous solution of NaOH 0.1 M were added dropwise under vigorous stirring to 50 mL of an aqueous solution of $Zn(NO_3)_2$ 0.1 M pre-heated at 30 °C, in an oil bath. The reaction was carried out for 24 h, keeping the temperature constant at 30 °C. The final suspension was

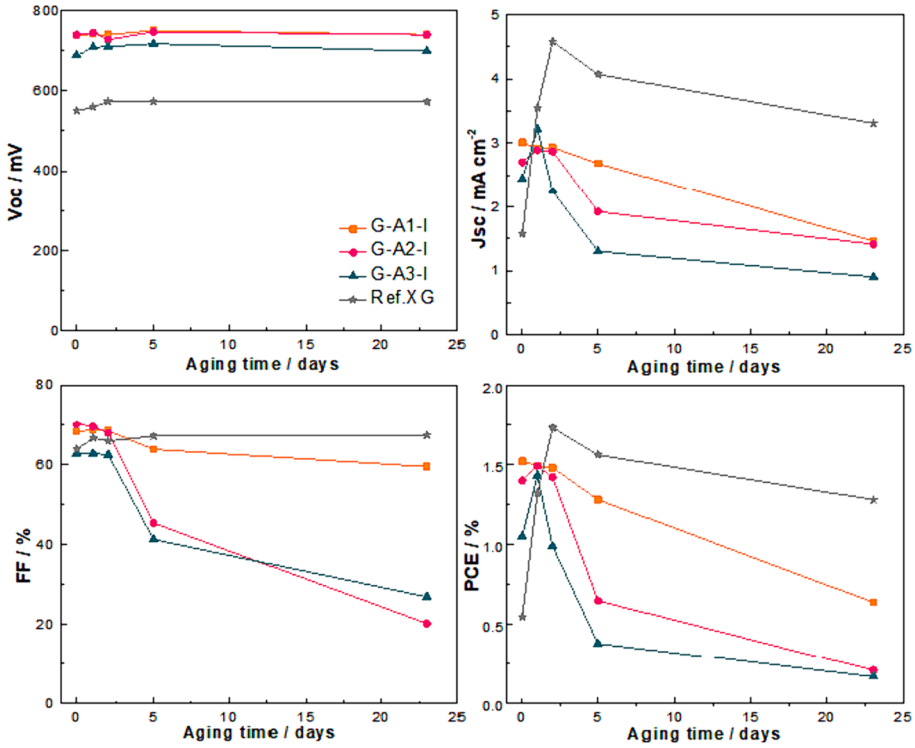

Fig. 7. Ageing time (V_{oc}, J_{sc}, FF and PCE) for the DSSC prepared with sulphur gels and reference XG gel, under 1 sun illumination.

centrifuged at 3000 rpm for 10 min and the precipitate washed once with deionized water. The drying of the precipitate overnight carried out in an oven at 30 °C yielded $Zn(OH)_2$, whereas if it was carried out at 50 °C, it yielded ZnO.

3.3. Structural and morphological characterization

The samples were characterized by XRD diffraction, using an X' pert pro X-ray diffractometer by Philips, operated with Cu K_α radiation. Diffraction profiles were analyzed with GSAS-II software according to Rietveld fitting procedures, that refines peak intensities and crystal cell edges (Å) of the phase. The Single-crystal phase data used for the Rietveld fitting (see above) were collected from the American Mineralogist Crystal Structure Database [77] or directly from the references reported above [43–46,54] as CIF files. Model powder patterns for Cu K_α wavelength (1.54 Å) were calculated as a convolution of modified asymmetric pseudo-Voigt functions centred on the experimental reflections [78] for each sample. The amorphous background due to galactomannan was measured at the same counting time and was subtracted from the total pattern. Infrared spectra were recorded with a Shimadzu Prestige-21 FT-IR instrument, equipped with an attenuated total reflectance (ATR) diamond crystal (Specac Golden Gate), in the 400–4000 cm^{-1} range, with a resolution of 4 cm^{-1}.

The surface morphology of the synthesized particles was determined with a FE-SEM, Field Emission Scanning Electron Microscope SUPRA TM 35, Carl Zeiss SMT, Oberkochen (Germany) operating at voltages between 1.5 and 7 kV. The freeze drying of the gel samples was carried out for 5 h at −61.5 °C and 330 Torr. The resulting powder was deposited on a silicon sample-holder and metallized by Au deposition.

Thermogravimetric analysis (TGA) data were recorded with a TA instruments Q600 thermobalance under dry N_2 flow (100 mL/min) with a ramp of 10 °C/min from RT to 150 °C.

3.4. Methods

FTO glass was cut in pieces (2 cm x 1.5 cm) and used as substrate for the fabrication of photoanodes and counter electrodes. They were washed in an ultrasonic bath (~15 min) with acetone and then EtOH and finally dried with technical paper. The photoanodes were prepared using a transparent TiO_2 paste, (18NR-T from Dyesol©) by screen-printing technique on the conductive side, leading to ~ 6 μm-thick electrode (0.5 cm × 0.5 cm active area). The electrodes underwent a sintering process at 450 °C for 30 min and they are let cooling down to room temperature slowly. Then they were dipped into a solution of $TiCl_4$ (40 mM in DI-H_2O) for 30 min at 70 °C and then rinsed with DI-H_2O and EtOH. The obtained electrodes underwent an additional sintering step up to 450 °C for 30 min, then cooled down to 70 °C and soaked into the dye solution. Dye solution was made of D131 dye (0.5 mM) and CDCA, as co-adsorbents (ratio 1:18 dye to CDCA) in a mixture of ACN/t-BuOH 1:1. Sensitization step was carried out at 25 °C for 4 h under dark conditions and shaking at 180 rpm in a Büchi Syncore type Q-101 (CH-9230 Flawil, Switzerland). After this, sensitized photoanodes were rinsed in EtOH. In the case of counter electrodes preparation, 40 μl of H_2PtCl_6 (5.0 mM solution in isopropanol) was drop casted onto the conductive side of an FTO substrate and heated up to 450 °C for 30 min. The reference aqueous gel electrolyte based on xanthan gum was prepared as previously reported [63]. Briefly, a saturated solution of CDCA in DI-H_2O was stirred overnight at 40 °C, then cooled to room temperature and filtered with paper, to remove the excess of CDCA. Then NaI (0.5 M) and I_2 (30 mM) were dissolved into the solution by stirring for 2 h; finally, xanthan gum powder (3 wt%) was added into the solution under stirring for 2 h at 40 °C, until a gel was obtained.

On the other hand, Zn-GM-based gels were prepared in advance and collected into different vials, at approximately the same volume. Every vial was weighed before and after the filling with the gel. The volume occupied by the gel in the vial, given the foamy nature of the system, could be only estimated by visual comparison with vials filled with pure water that were successively weighed. The addition of the redox couple I_3^-/I_2 was accomplished according to the molar ratios employed for the Ref XG, that amount to 73.6 mg of NaI (as iodide anion source) and to 7.6 mg of iodine for every ml of the gel, corresponding to concentrations 0.5 M and 0.03 M for iodide and iodine, respectively. The weighed

quantities of the two components of the redox mediator were scaled to respect the ratio if the volume of the gel sample were different. After the addition, the gels were vortexed at high speed for at least 10 min, in order to homogenize the mixtures that turned dark orange at the end of the mixing. In any case, the samples maintained a good gelly consistency, only a little bit wetter. All the gel aqueous electrolytes were stored in dark condition at room temperature.

3.5. Cells assembly

Gel aqueous electrolyte (~2.5 mg) was cast on the pre-dyed TiO_2 layer (active area 0.25 cm^2) with a spatula; the photoanode and counter electrode were then glued together with a Surlyn© thermoplastic film (internal square area = 0.6 x 0.6 cm^2) by hot pressing (20 s) at 105 °C (~50 μm as definitive interelectrode distance). In symmetric devices, two counter-electrodes (or two pristine FTO glasses) are glued together following the above reported procedure, in which the photoanode is replaced by a Pt/FTO electrode.

3.6. Electrochemical characterization

Current-voltage (J-V curves) parameters and stability data for complete devices were measured with a solar simulator (ABET Technologies Inc, model 10500, Milford USA) under 1 sun light intensity (0.1 W/cm2, AM 1.5G) equipped with a 150 W xenon arc lamp and connected to a digital source meter unit (SMU 2420 Keithley, Tektronix, USA), after calibration with a silicon reference solar cell (irradiation sensor, Spektron 210, 74.63 mV).

Electrochemical impedance spectroscopy (EIS) data were recorded using a potentiostat (SP-150 BioLogic) in the frequency range between 100 kHz and 10 mHz. The amplitude of the AC signal was 10 mV. Spectra were recorded under dark conditions for symmetric devices at 0 mV.

The transmittance data were recorded with UV–Visible spectrophotometer (Varian Cary 300 Bio, Series II, Agilent technologies, Australia) in the wavelength range of 300–800 nm, for the complete cells and for FTO/gel/FTO.

4. Conclusions

In this contribution, we implemented Zn-based nanostructures as gelling agent for aqueous Quasi-Solid Electrolytes (QSE) for Dye Sensitized Solar Cells (DSSCs) according to an entirely biocompatible protocol. The synthetic procedures comprise only environmentally friendly substances, namely water solutions of the natural polysaccharide galactomannan and zinc-based non-toxic inorganic salts as gelling agents. All the reactions were carried out in user-friendly and sustainable conditions at room temperature or 40 °C at maximum, and small ethanol quantities in the final workup of the products. Neither use of Volatile Organic Compounds (VOCs) nor production of harmful waste took place in the whole procedure. Depending on the specific inorganic salt employed, the resulting hydrogel contains either hydrosulphate lamellae or oxide nanoparticles, as it was ascertained by means of XRD, IR spectroscopy and SEM microscopy analyses. Using either I-loaded gel as quasi-solid electrolyte, well performing DSSC devices could be setup, that showed a remarkably high photovoltage, around 750 mV, i.e. significantly higher than reference hydrogels, and state-of the-art PCE (~2%), the main limiting factor being the charge diffusion as indicated by the EIS analyses. In the case of hydroxysulfate gelator, the cells have the added value of a noteworthy transparency, exhibiting, in the best case, a very promising AVT up to 22 %. The LUE reaches 0.35 %, i.e. more than double than the xanthan gum device, used as reference. Finally, LR-TDDFT simulations on a model iodine/iodide layered zinc hydroxy sulphate structure account for the general blueshift of the UV–Vis absorption spectra, in accordance with the AVT observations. In general, the intrinsic lightness and flexibility of these materials could be conveniently exploited in future applications in the field of building and vehicle integration, agrivoltaics and aerospace. Overall, this work testifies how the perfect match between bio-based and inorganic world can lead to highest-level outcomes of technological interest.

Conflicts of interest

There are no conflicts to declare.

Funding

CPU computing time was granted by the “Excellence-2018” Program (Dipartimenti di Eccellenza) of the Italian Ministry of Research, DIBAF-Department of University of Tuscia, Project “**Landscape 4.0**—food, wellbeing and environment” (Nico Sanna). A.Y.S.Z, S.G., C.B and M.B. acknowledge support from the Project **CH4.0** under the MUR program “Dipartimenti di Eccellenza 2023–2027” (CUP D13C22003520001). S. G. acknowledges the project NODES which has received funding from the MUR - M4C2 1.5 of PNRR founded by the European Union - NextGenerationEU (Grant Agreement no. ECS00000036). C.B. M.B. acknowledges support from the Project **BEST4U** under the grant FESR, PON Ricerca e Innovazione 2014-2020, Project n. ARS01_00519. A.Y.S. Z. acknowledges the support by the Technological Institute of Costa Rica under the grant No. 65-2018-D. M.C, L.G. and E.M.B. acknowledge the project PRIN2022 2022F4YZP9 **“GREEN^3**. L.G. and M.C acknowledge support from the Project **X-CHEM** under the MUR program “Dipartimenti di Eccellenza 2023–2027” (CUP E83C23000340006). Support from Prof. A. Latini (Rome Sapienza University, Chemistry Department) is acknowledged for some XRD spectra recording.

CRediT authorship contribution statement

Ana Yancy Segura Zarate: Data curation, Formal analysis, Investigation, Validation. **Lorenzo Gontrani:** Data curation, Formal analysis, Investigation, Resources, Software, Validation, Writing – original draft, Writing – review & editing. **Simone Galliano:** Investigation, Validation, Writing – original draft. **Elvira Maria Bauer:** Data curation, Formal analysis, Investigation. **Domenica Tommasa Donia:** Data curation, Formal analysis, Investigation, Validation. **Claudia Barolo:** Funding acquisition, Project administration, Writing – review & editing. **Matteo Bonomo:** Conceptualization, Funding acquisition, Methodology, Resources, Supervision, Visualization, Writing – original draft, Writing – review & editing. **Marilena Carbone:** Conceptualization, Formal analysis, Methodology, Funding acquisition, Project administration, Resources, Supervision, Visualization, Writing – original draft, Writing – review & editing.

Declaration of competing interest

The authors declare that they have no known competing financial interests or personal relationships that could have appeared to influence the work reported in this paper.

Appendix A. Supplementary data

Summary of synthesis parameters, Powder X-Ray Diffraction patterns of G-B2 and of galactomannan, Galactomannan IR spectrum, Weight loss plots of the nanocomposite hydrogels, J-V curves of the devices, Nyquist plots of symmetric Pt-Pt devices based on G-AX-I electrolytes and ref XG, UV-Vis spectra of complete cell, Sketch of Namuwite crystal structure, ab initio model of iodine molecule - sulphate anion interaction. Theoretical UV-Vis spectrum of I_2 and SO_4—I_2 complexes. Supplementary data to this article can be found online at https://doi.org/10.1016/j.solener.2024.112460.

References

[1] B. O'Regan, M. Grätzel, A low-cost, high-efficiency solar cell based on dye-sensitized colloidal TiO_2 films, Nature 353 (1991) 737–740, https://doi.org/10.1038/353737a0.

[2] R. Haridas, J. Velore, S.C. Pradhan, A. Vindhyasarumi, K. Yoosaf, S. Soman, K.N. N. Unni, A. Ajayaghosh, Indoor light-harvesting dye-sensitized solar cells surpassing 30% efficiency without co-sensitizers, Mater. Adv. 2 (2021) 7773–7787, https://doi.org/10.1039/D1MA00829C.

[3] J.H. Kim, K.J. Moon, J.M. Kim, D. Lee, S.H. Kim, Effects of various light-intensity and temperature environments on the photovoltaic performance of dye-sensitized solar cells, Sol. Energy 113 (2015) 251–257, https://doi.org/10.1016/j.solener.2015.01.012.

[4] H. Michaels, M. Rinderle, R. Freitag, I. Benesperi, T. Edvinsson, R. Socher, A. Gagliardi, M. Freitag, Dye-sensitized solar cells under ambient light powering machine learning: towards autonomous smart sensors for the internet of things, Chem. Sci. 11 (2020) 2895–2906, https://doi.org/10.1039/C9SC06145B.

[5] M. Szindler, M. Szindler, A. Drygała, K. Lukaszkowicz, P. Kaim, R. Pietruszka, Dye-sensitized solar cell for building-integrated photovoltaic (BIPV) applications, Materials 14 (2021) 3743, https://doi.org/10.3390/ma14133743.

[6] S. Sasidharan, S.C. Pradhan, A. Jagadeesh, B.N. Nair, A.A.P. Mohamed, N.U. K. N, S. Soman, U.N.S. Hareesh, Bifacial Dye-Sensitized Solar Cells with Enhanced Light Scattering and Improved Power Conversion Efficiency under Full Sun and Indoor Light Conditions, ACS Appl. Energy Mater. 3 (2020) 12584–12595. https://doi.org/10.1021/acsaem.0c02500.

[7] F. Grifoni, M. Bonomo, W. Naim, N. Barbero, T. Alnasser, I. Dzeba, M. Giordano, A. Tsaturyan, M. Urbani, T. Torres, C. Barolo, F. Sauvage, Toward sustainable, colorless, and Transparent photovoltaics: state of the art and perspectives for the development of selective Near-Infrared dye-sensitized Solar cells, Adv. Energy Mater. 11 (2021) 2101598, https://doi.org/10.1002/aenm.202101598.

[8] D. Ursu, M. Vajda, M. Miclau, Highly efficient dye-sensitized solar cells for wavelength-selective greenhouse: a promising agrivoltaic system, Int. J. Energy Res. 46 (2022) 18550–18561, https://doi.org/10.1002/er.8469.

[9] A. Ghosh, Fenestration integrated BIPV (FIPV): a review, Sol. Energy 237 (2022) 213–230, https://doi.org/10.1016/j.solener.2022.04.013.

[10] B. Commault, T. Duigou, V. Maneval, J. Gaume, F. Chabuel, E. Voroshazi, Overview and perspectives for vehicle-integrated photovoltaics, Appl. Sci. 11 (2021) 11598, https://doi.org/10.3390/app112411598.

[11] M. Nagata, E. Baldwin, S. Kim, M. Taya, Design of dye-sensitized solar cells integrated in composite panel subjected to bending, J. Compos. Mater. 47 (2013) 27–32, https://doi.org/10.1177/0021998312459779.

[12] S.G. Bailey, J.D. Harris, A.F. Hepp, E.J. Anglin, R.P. Raffaelle, H.R. Clark, S.T.P. Gardner, S.S. Sun, Thin-film organic-based solar cells for space power, in: IECEC '02. 2002 37th Intersociety Energy Conversion Engineering Conference, 2002., IEEE, n.d.: pp. 191–196. https://doi.org/10.1109/IECEC.2002.1392006.

[13] N. Mariotti, M. Bonomo, L. Fagiolari, N. Barbero, C. Gerbaldi, F. Bella, C. Barolo, Recent advances in eco-friendly and cost-effective materials towards sustainable dye-sensitized solar cells, Green Chem. 22 (2020) 7168–7218, https://doi.org/10.1039/D0GC01148G.

[14] L. Mauri, A. Colombo, C. Dragonetti, F. Fagnani, A fascinating trip into iron and copper dyes for DSSCs, Inorganics (Basel) 10 (2022) 137, https://doi.org/10.3390/inorganics10090137.

[15] E. Marchini, M. Orlandi, N. Bazzanella, R. Boaretto, V. Cristino, A. Miotello, S. Caramori, S. Carli, Electrodeposited PEDOT/Nafion as catalytic counter electrodes for cobalt and copper bipyridyl redox mediators in dye-sensitized solar cells, ACS Omega 7 (2022) 29181–29194, https://doi.org/10.1021/acsomega.2c03229.

[16] J.-H. Kim, D.-H. Kim, J.-H. So, H.-J. Koo, Toward eco-friendly dye-sensitized solar cells (DSSCs): natural dyes and aqueous electrolytes, Energies (Basel) 15 (2021) 219, https://doi.org/10.3390/en15010219.

[17] C. Law, S.C. Pathirana, X. Li, A.Y. Anderson, P.R.F. Barnes, A. Listorti, T. H. Ghaddar, B.C. O'Regan, Water-based electrolytes for dye-sensitized solar cells, Adv. Mater. 22 (2010) 4505–4509, https://doi.org/10.1002/adma.201001703.

[18] S. Galliano, F. Bella, G. Piana, G. Giacona, G. Viscardi, C. Gerbaldi, M. Grätzel, C. Barolo, Finely tuning electrolytes and photoanodes in aqueous solar cells by experimental design, Sol. Energy 163 (2018) 251–255, https://doi.org/10.1016/j.solener.2018.02.009.

[19] D. Spadaro, J. Barichello, I. Citro, G. Calogero, Environmentally friendly water-based electrolyte for dye-sensitized Solar cells: future prospective and outlook, Solar 3 (2023) 229–252, https://doi.org/10.3390/solar3020015.

[20] F. Bella, S. Galliano, M. Falco, G. Viscardi, C. Barolo, M. Grätzel, C. Gerbaldi, Unveiling iodine-based electrolytes chemistry in aqueous dye-sensitized solar cells, Chem. Sci. 7 (2016) 4880–4890, https://doi.org/10.1039/C6SC01145D.

[21] K.A. Kamenan, A. Jagadeesh, N.R. Kre, E.F. Assanvo, S. Soman, K.N.N. Unni, Natural rubber (Hevea Brasiliensis)-based quasi-solid electrolyte as a potential candidate for arresting recombination and improving performance in aqueous dye-sensitized solar cells, J. Mater. Sci. Mater. Electron. 32 (2021) 14207–14216, https://doi.org/10.1007/s10854-021-05979-3.

[22] C. Law, O. Moudam, S. Villarroya-Lidon, B. O'Regan, Managing wetting behavior and collection efficiency in photoelectrochemical devices based on water electrolytes; improvement in efficiency of water/iodide dye sensitised cells to 4%, J. Mater. Chem. 22 (2012) 23387, https://doi.org/10.1039/c2jm35245a.

[23] M. Kaneko, T. Nomura, C. Sasaki, Photoinduced Charge Separation in an aqueous phase using nanoporous TiO2 film and a quasi-solid made of natural products, Macromol. Rapid Commun. 24 (2003) 444–446, https://doi.org/10.1002/marc.200390059.

[24] X. Liu, Z. Mao, J. Liu, F. Meng, X. Shi, X. Xue, B. Zhao, Probing the open-circuit voltage improvement of DSSC via Raman spectroscopy. *in situ* dynamic tracking photoanode/electrolyte interfaces, ACS Appl. Energy Mater. 5 (2022) 8391–8399, https://doi.org/10.1021/acsaem.2c00924.

[25] S. Borbón, S. Lugo, D. Pourjafari, N. Pineda Aguilar, G. Oskam, I. López, Open-circuit voltage (VOC) enhancement in TiO2-based DSSCs: incorporation of ZnO nanoflowers and Au Nanoparticles, ACS Omega 5 (2020) 10977–10986, https://doi.org/10.1021/acsomega.0c00794.

[26] O.O. Ogunsolu, J.C. Wang, K. Hanson, Increasing the open-circuit voltage of dye-sensitized solar cells via metal-ion coordination, Inorg. Chem. 56 (2017) 11168–11175, https://doi.org/10.1021/acs.inorgchem.7b01531.

[27] T.W. Hamann, R.A. Jensen, A.B.F. Martinson, H. Van Ryswyk, J.T. Hupp, Advancing beyond current generation dye-sensitized solar cells, Energy Environ. Sci. 1 (2008) 66, https://doi.org/10.1039/b809672d.

[28] V. Leandri, H. Ellis, E. Gabrielsson, L. Sun, G. Boschloo, A. Hagfeldt, An organic hydrophilic dye for water-based dye-sensitized solar cells, Phys. Chem. Chem. Phys. 16 (2014) 19964–19971, https://doi.org/10.1039/C4CP02774D.

[29] H. Zhang, L. Qiu, D. Xu, W. Zhang, F. Yan, Performance enhancement for water based dye-sensitized solar cells via addition of ionic surfactants, J. Mater. Chem. A 2 (2014) 2221–2226, https://doi.org/10.1039/C3TA14571A.

[30] R.S. Shaikh, R.B. Rajput, R.B. Kale, Inexpensive green synthesis of natural dye-sensitized solar cells with aqueous solution as a Bi2S3 counter electrode, Next Mater. 3 (2024) 100051, https://doi.org/10.1016/j.nxmate.2023.100051.

[31] H. Choi, B.-S. Jeong, K. Do, M.J. Ju, K. Song, J. Ko, Aqueous electrolyte based dye-sensitized solar cells using organic sensitizers, New J. Chem. 37 (2013) 329–336, https://doi.org/10.1039/C2NJ40577F.

[32] J. Wu, Z. Lan, J. Lin, M. Huang, Y. Huang, L. Fan, G. Luo, Electrolytes in dye-sensitized Solar cells, Chem. Rev. 115 (2015) 2136–2173, https://doi.org/10.1021/cr400675m.

[33] V.L. Finkenstadt, Natural polysaccharides as electroactive polymers, Appl. Microbiol. Biotechnol. 67 (2005) 735–745, https://doi.org/10.1007/s00253-005-1931-4.

[34] M.M. Hasan, M.D. Islam, T.U. Rashid, Biopolymer-based electrolytes for dye-sensitized Solar cells: a critical review, Energy Fuels 34 (2020) 15634–15671, https://doi.org/10.1021/acs.energyfuels.0c03396.

[35] B. Selvaraj, G. Shanmugam, S. Kamaraj, E. Thirugnanasambandam, A. Gunasekeran, A. Sambandam, Effect of an aqueous copper gel electrolyte with cobalt metal organic framework based additive on performance of aqueous-dye-sensitized solar cells, Sol. Energy 236 (2022) 586–598, https://doi.org/10.1016/j.solener.2022.03.034.

[36] A. Johnson Mary Leeda Rani, A. Gunasekeran, D. Sundaramurthy, A. Sambandam, Effect of a locust bean gum based gel electrolyte with nanocomposite additives on the performance of a dye-sensitized solar cell, New J. Chem. 46 (2022) 13156–13166. https://doi.org/10.1039/D2NJ02182J.

[37] J.L. Monteith, Solar radiation and productivity in tropical ecosystems, J. Appl. Ecol. 9 (1972) 747, https://doi.org/10.2307/2401901.

[38] P. Guleria, V. Kumar, E. Lichtfouse, eds., Sustainable Agriculture Reviews 45, Springer International Publishing, Cham, 2020. https://doi.org/10.1007/978-3-030-53017-4.

[39] J. Duan, H. Wen, S. Zong, T. Li, H. Lv, L. Liu, Soft/Hard controllable conversion galactomannan ionic conductive hydrogel as a flexible sensor, ACS Appl. Electron. Mater. 3 (2021) 5000–5014, https://doi.org/10.1021/acsaelm.1c00795.

[40] D.T. Donia, E.M. Bauer, M. Missori, L. Roselli, D. Cecchetti, P. Tagliatesta, L. Gontrani, M. Carbone, Room temperature syntheses of ZnO and their structures, Symmetry (Basel) 13 (2021) 733, https://doi.org/10.3390/sym13040733.

[41] S. Wang, C. Xu, Z. Lei, J. Li, J. Lu, Q. Xiang, X. Chen, Y. Hua, Y. Li, Recycling of zinc oxide dust using ChCl-urea deep eutectic solvent with nitrilotriacetic acid as complexing agents, Miner. Eng. 175 (2022) 107295, https://doi.org/10.1016/j.mineng.2021.107295.

[42] B.H. Toby, R.B. Von Dreele, GSAS-II : the genesis of a modern open-source all purpose crystallography software package, J. Appl. Crystallogr. 46 (2013) 544–549, https://doi.org/10.1107/S0021889813003531.

[43] N.V. Chukanov, R.K. Rastsvetaeva, S.M. Aksenov, I.V. Pekov, D.I. Belakovskiy, G. Blass, G. Möhn, Lahnsteinite, Zn4(SO4)(OH)6 · 3H2O, a new mineral from the Friedrichssegen Mine, Germany, Geol. Ore Dep. 55 (2013) 663–668, https://doi.org/10.1134/S1075701513080023.

[44] L.A. Groat, The crystal structure of namuwite, a mineral with Zn in tetrahedral and octahedral coordination, and its relationship to the synthetic basic zinc sulfates, Am. Miner. 81 (1996) 238–243, https://doi.org/10.2138/am-1996-1-229.

[45] I.J. Bear, I.E. Grey, I.C. Madsen, I.E. Newnham, L.J. Rogers, Structures of the basic zinc sulfates 3Zn(OH)2.ZnSO4. mH2O, m = 3 and 5, Acta Crystallogr. B 42 (1986) 32–39, https://doi.org/10.1107/S0108768186098622.

[46] M. Ohnishi, I. Kusachi, S. Kobayashi, Osakaite, $Zn_4SO_4(OH)_6 \cdot 5H_2O$, A New Mineral Species From The Hirao Mine, Osaka, Japan, Can. Mineral. 45 (2007) 1511–1517. https://doi.org/10.3749/canmin.45.6.1511.

[47] S.J. Mills, F. Hatert, E.H. Nickel, G. Ferraris, The standardisation of mineral group hierarchies: application to recent nomenclature proposals, Eur. J. Mineral. 21 (2009) 1073–1080, https://doi.org/10.1127/0935-1221/2009/0021-1994.

[48] G. Arizaga, K. Satyanarayana, F. Wypych, Layered hydroxide salts: synthesis, properties and potential applications, Solid State Ion. 178 (2007) 1143–1162, https://doi.org/10.1016/j.ssi.2007.04.016.

[49] L. Gontrani, D.T. Donia, E. Maria Bauer, P. Tagliatesta, M. Carbone, Novel synthesis of zinc oxide Nanoparticles from type IV deep eutectic solvents, Inorg. Chim. Acta 545 (2023) 121268, https://doi.org/10.1016/j.ica.2022.121268.

[50] L.S. Germann, R.E. Dinnebier, X. Liu, Y. Dong, W. Li, On the crystal structure of a previously unknown anhydrous zinc hydroxide sulfate, Z. Anorg. Allg. Chem. 642 (2016) 255–259, https://doi.org/10.1002/zaac.201500774.
[51] J. Demel, J. Hynek, P. Kovář, Y. Dai, C. Taviot-Guého, O. Demel, M. Pospíšil, K. Lang, Insight into the structure of layered zinc hydroxide salts intercalated with dodecyl sulfate anions, J. Phys. Chem. C 118 (2014) 27131–27141, https://doi.org/10.1021/jp508499g.
[52] T. Stanimirova, T. Kerestedjian, G. Kirov, Dehydration and rehydration of Zn-hydroxy sulfate minerals with interrupted decorated hydroxide sheets, Appl. Clay Sci. 135 (2017) 16–26, https://doi.org/10.1016/j.clay.2016.08.032.
[53] D.A. Leal, G. Machado Silva, J. Tedim, F. Wypych, C.E.B. Marino, Synthesis and characterization of gordaite, osakaite and simonkolleite by different methods: Comparison, phase interconversion, and potential corrosion protection applications, J. Solid State Chem. 291 (2020) 121595, https://doi.org/10.1016/j.jssc.2020.121595.
[54] Z. Delcheva, T. Stanimirova, N. Petrova, Order of osakaite–namuwite–lahnsteinite formation during alkalization of sulfate solutions, Rev. Bulg. Geol. Soc. 83 (2022) 51–61. https://doi.org/10.52215/rev.bgs.2022.83.2.51.
[55] A.S. Kazachenko, Y.N. Malyar, S. Ghatfaoui, N. Issaoui, O. Al-Dossary, M.J. Wojcik, A.S. Kazachenko, A.V. Miroshnikova, Y.D. Berezhnaya, A density functional theory calculations of infrared spectra of galactomannan butyl ether, J. Mol. Struct. 1251 (2022) 131998, https://doi.org/10.1016/j.molstruc.2021.131998.
[56] K. Nakamoto, Infrared and Raman spectra of inorganic and coordination compounds, Wiley (2008), https://doi.org/10.1002/9780470405840.
[57] V.O. Fasiku, C.A. Omolo, N. Devnarain, U.H. Ibrahim, S. Rambharose, M. Faya, C. Mocktar, S.D. Singh, T. Govender, Chitosan-based hydrogel for the dual delivery of antimicrobial agents against bacterial methicillin-resistant *Staphylococcus aureus* biofilm-infected wounds, ACS Omega 6 (2021) 21994–22010, https://doi.org/10.1021/acsomega.1c02547.
[58] R. Singh, N.A. Jadhav, S. Majumder, B. Bhattacharya, P.K. Singh, Novel biopolymer gel electrolyte for dye-sensitized solar cell application, Carbohydr. Polym. 91 (2013) 682–685, https://doi.org/10.1016/j.carbpol.2012.08.055.
[59] S.S. Soni, K.B. Fadadu, R.L. Vekariya, J. Debgupta, K.D. Patel, A. Gibaud, V. K. Aswal, Effect of self-assembly on triiodide diffusion in water based polymer gel electrolytes: an application in dye solar cell, J. Colloid Interface Sci. 425 (2014) 110–117, https://doi.org/10.1016/j.jcis.2014.03.047.
[60] K.K. Sonigara, H.K. Machhi, J.V. Vaghasiya, A. Gibaud, S.C. Tan, S.S. Soni, A Smart flexible solid state photovoltaic Device with Interfacial cooling recovery feature through thermoreversible Polymer gel electrolyte, Small 14 (2018), https://doi.org/10.1002/smll.201800842.
[61] F. Bella, S. Galliano, M. Falco, G. Viscardi, C. Barolo, M. Grätzel, C. Gerbaldi, Approaching truly sustainable solar cells by the use of water and cellulose derivatives, Green Chem. 19 (2017) 1043–1051, https://doi.org/10.1039/C6GC02625G.
[62] J.C. de Haro, E. Tatsi, L. Fagiolari, M. Bonomo, C. Barolo, S. Turri, F. Bella, G. Griffini, Lignin-based Polymer electrolyte membranes for sustainable aqueous dye-sensitized Solar cells, ACS Sustain. Chem. Eng. 9 (2021) 8550–8560, https://doi.org/10.1021/acssuschemeng.1c01882.
[63] S. Galliano, F. Bella, M. Bonomo, G. Viscardi, C. Gerbaldi, G. Boschloo, C. Barolo, Hydrogel electrolytes based on xanthan gum: green route towards stable dye-sensitized Solar cells, Nanomaterials 10 (2020) 1585, https://doi.org/10.3390/nano10081585.
[64] M. Bonomo, A.Y. Segura Zarate, L. Fagiolari, A. Damin, S. Galliano, C. Gerbaldi, F. Bella, C. Barolo, Unreported resistance in charge transport limits the photoconversion efficiency of aqueous dye-sensitised solar cells: an electrochemical impedance spectroscopy study, Mater. Today Sustain. 21 (2023) 100271, https://doi.org/10.1016/j.mtsust.2022.100271.
[65] M. Bonomo, A. Di Carlo, D. Dini, Study of the influence of the I-based electrolyte composition on the photoconversion properties of p-type dye-sensitized Solar cells, J. Electrochem. Soc. 165 (2018) H889–H896, https://doi.org/10.1149/2.0261814jes.
[66] J. Cong, X. Yang, Y. Hao, L. Kloo, L. Sun, A highly efficient colourless sulfur/iodide-based hybrid electrolyte for dye-sensitized solar cells, RSC Adv 2 (2012) 3625, https://doi.org/10.1039/c2ra20310c.
[67] W. Naim, F. Grifoni, V. Challuri, D. Mathiron, S. Ceurstemont, P. Chotard, T. Alnasser, I. Dzeba, N. Barbero, S. Pilard, C. Barolo, F. Sauvage, Hybrid sulfurothioate-based electrolyte improving aesthetics, performance, and stability of transparent NIR-dye-sensitized solar cells, Cell Rep. Phys. Sci. 4 (2023) 101455, https://doi.org/10.1016/j.xcrp.2023.101455.
[68] Y. Zhao, D.G. Truhlar, The M06 suite of density functionals for main group thermochemistry, thermochemical kinetics, noncovalent interactions, excited states, and transition elements: two new functionals and systematic testing of four M06-class functionals and 12 other functionals, Theor. Chem. Acc. 120 (2008) 215–241, https://doi.org/10.1007/s00214-007-0310-x.
[69] T. Yanai, D.P. Tew, N.C. Handy, A new hybrid exchange–correlation functional using the Coulomb-attenuating method (CAM-B3LYP), Chem. Phys. Lett. 393 (2004) 51–57, https://doi.org/10.1016/j.cplett.2004.06.011.
[70] A. Siiskonen, A. Priimagi, Benchmarking DFT methods with small basis sets for the calculation of halogen-bond strengths, J. Mol. Model. 23 (2017) 50, https://doi.org/10.1007/s00894-017-3212-4.
[71] W. Chen, Y. Qiu, K. Yan, S. Yang, Surfactant directed self-assembly of size-tunable mesoporous titanium dioxide microspheres and their application in quasi-solid state dye-sensitized solar cells, J. Power Sources 196 (2011) 10806–10816, https://doi.org/10.1016/j.jpowsour.2011.09.011.
[72] E. Raphael, D.H. Jara, M.A. Schiavon, Optimizing photovoltaic performance in CuInS2 and CdS quantum dot-sensitized solar cells by using an agar-based gel polymer electrolyte, RSC Adv. 7 (2017) 6492–6500, https://doi.org/10.1039/C6RA27635K.
[73] O. Długosz, Natural deep eutectic solvents in the synthesis of inorganic Nanoparticles, Materials 16 (2023) 627, https://doi.org/10.3390/ma16020627.
[74] M. Carbone, S. De Rossi, D.T. Donia, G. Di Marco, B. Gustavino, L. Roselli, P. Tagliatesta, A. Canini, A. Gismondi, Biostimulants promoting growth of Vicia faba L. seedlings: inulin coated ZnO nanoparticles, Chem. Biol. Technol. Agric. 10 (2023) 134, https://doi.org/10.1186/s40538-023-00507-3.
[75] L. Gontrani, E.M. Bauer, L. Casoli, C. Ricci, A. Lembo, D.T. Donia, S. Quaranta, M. Carbone, Inulin-coated ZnO Nanoparticles: a Correlation between Preparation and properties for biostimulation purposes, Int. J. Mol. Sci. 25 (2024) 2703, https://doi.org/10.3390/ijms25052703.
[76] E.M. Bauer, A. Talone, P. Imperatori, R. Briancesco, L. Bonadonna, M. Carbone, The addition of Co into CuO–ZnO oxides triggers high antibacterial activity and low cytotoxicity, Nanomaterials 13 (21) (2023) 2823, https://doi.org/10.3390/nano13212823.
[77] R.T. Downs, M. Hall-Wallace, The American mineralogist crystal structure database, Am. Mineral. 88 (2003) 247–250.
[78] L.W. Finger, D.E. Cox, A.P. Jephcoat, A correction for powder diffraction peak asymmetry due to axial divergence, J. Appl. Crystallogr. 27 (1994) 892–900, https://doi.org/10.1107/S0021889894004218.